HIGH RESOLUTION OBLIQUE IMPACT SIMULATIONS OF THE FORMATION OF THE SOUTH POLE-AITKEN BASIN. T. M. Davison, N. Baijal and G. S. Collins. Impacts & Astromaterials Research Centre, Dept of Earth Science & Engineering, Imperial College London, London, SW7 2AZ, UK (E-mail: thomas.davison@imperial.ac.uk).

Introduction: The 2500-km diameter South Pole-Aitken (SPA) basin is the largest known impact structure in the Solar System. The effects on the Moon of this giant impact were profound. The crater dominates the topography, crustal structure, surface composition and subsurface density distribution of the lunar farside and South Pole [1–3].

As the oldest preserved impact basin on the Moon, SPA lies stratigraphically beneath all other basins. Understanding the timing and formation of the SPA basin is therefore key to unlocking much of the Moon's history and evolution. Previous 2D numerical simulations of the SPA impact [4] showed that its consequences are sensitive to the thermal state of the Moon at the time of impact and hence how soon after the Moon's formation the collision occurred. Numerical modeling of the formation of SPA offers a potential way to constrain the thermal state of the Moon at the time of impact and thereby illuminate the Moon's earliest history of bombardment [5]. Numerical modeling can also be used to predict the spatial distribution of ejecta, the depth from which mantle materials were exposed during the impact, and the fate of the impactor, which have implications for interpreting the Moon's compositional and geophysical anomalies [3, 6, 7].

Under the simplifying assumption of a vertical impact, [4] proposed a model for SPA's formation in which a 170 km diameter rocky impactor struck a hot Moon with a steep near-surface thermal gradient (50 K/km) at a velocity of 10 km/s. This model gave the best match to the SPA compositional anomaly and crustal structure derived from gravity data and produced a transient crater diameter of ∼850 km. SPA's elliptical planform and asymmetric surrounding topography, however, imply that the impact was oblique, with a trajectory approximately south to north [1]. Recent 3D models of SPA's formation, which have explored the consequence of SPA as an oblique impact, assumed a much cooler lunar interior, with a near-surface thermal gradient of 10 K/km representative of the Moon's thermal state ∼500 Myrs after its formation [6, 7]. Left unresolved is the combined role of impact angle, impact energy and lunar thermal state on the formation of the SPA basin. A model of SPA's formation consistent with all observational constraints therefore remains elusive.

Here we present results from new high-resolution 3D simulations of the formation of the SPA basin as an oblique impact that investigate the effect of different thermal profiles, and of including compositionally distinct layers in the Moon and the impactor, on final crater structure, ejecta production and impactor fate.

Modeling: The SPA impact was simulated using the iSALE3D shock physics code [8]. Two lunar thermal gradients were considered; the 50 K/km profile favored by previous 2D models [4] and a 10 K/km profile used in previous 3D modeling [6, 7]. To produce similar sized transient craters, we used the same impactor for both models with a velocity of 10 km/s with the hot profile and 15 km/s with the cold profile. Both models presented here used an impact angle of 45° and a 200-km diameter differentiated impactor, consisting of an iron core (33% by mass) and a dunite mantle. The Moon consisted of a 350 km radius iron core, a dunite mantle and a 50 km granitic crust. All materials were described by ANEOS-derived equation of state tables [9–12] and strength models used by [4].

Simulation of SPA-scale impacts to late times with a differentiated impactor required the development of additional functionality in iSALE3D to calculate multiple

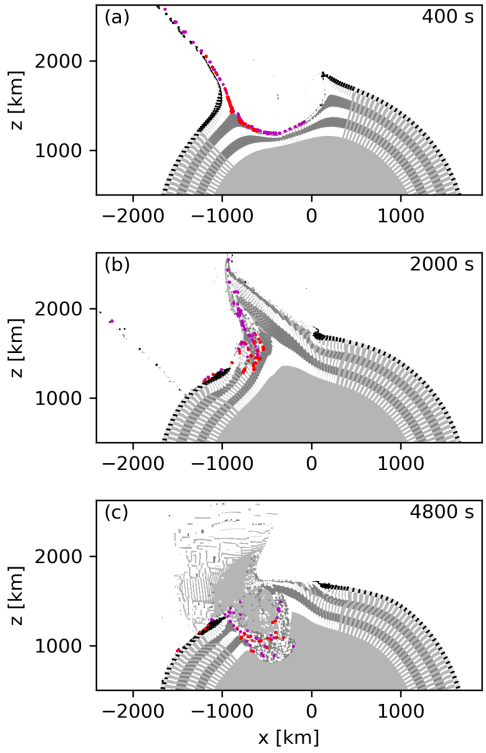

Figure 1: Slices along the symmetry plane for the 15 km/s; 10 K/km model. Red and purple tracers represent impactor core and mantle, respectively. Black tracers represent the 50 km thick lunar crust. Grey and white tracers represent layers of 100 km thickness in the upper mantle. (a) The time of the transient crater. (b) The time of maximum uplift. (c) After collapse of the central uplift.

interfaces per cell, and modify the material fluxes accordingly, as well as improvements to iSALE3D's parallel performance. These developments allowed a mesh resolution of 5 km per cell (20 cells per impactor radius) to be employed here, equivalent to the resolution used in previous 2D SPA simulations [4] and 2–4 times higher than previous 3D SPA simulations [6, 7].

Lagrangian tracer particles in the impactor and target tracked cratering motions. In the impactor, tracer particles were placed in every cell. In the target, to reduce the total number of tracers, particles were placed on a spherical grid, with constant spacing in radius, azimuthal and polar angle. A higher-resolution cone contained the impact site and crater. The landing positions of ejected tracers were determined using ballistic projection.

Results: Figure 1 shows the evolution of the 15 km/s, 10 K/km (cold) SPA simulation during the first 80 minutes, showing the times of transient crater formation (a), maximum central uplift (b) and first collapse of the central uplift (c). The cold and hot SPA scenario simulations yield transient crater diameters of 1050 and 960 km, respectively, within the range considered by previous works [4, 6, 7]. The ellipticity (ratio of semimajor axis to semiminor axis) of the transient craters is ≈ 1.15 for both simulations, similar to the ellipticity of the outer topography of the SPA basin (1.17), but not as elliptical as the inner ellipse (1.35) [1]. This suggests a shallower impact angle may be required to match the observed ellipticity.

Approximate dimensions of the major structural features of the basin for comparison with observations are evident after collapse of the central uplift 2000–4800 s, despite cratering motions continuing beyond this time. The zone of excavated crust in the basin center is approximately 560 km radius in the cold simulation, and at least 480 km in radius in the hot simulation. This is consistent with the observed paucity of anorthositic material (i.e., upper crustal material) inside a radius of 630 km from the crater centre [13]. Similarly, the semimajor axis of the crater rim in the cold and hot simulation is ≈1350 km and 1250 km, respectively, within $\approx$ 10% of the size of the measured outer ellipse [1]. Moreover, $\approx 30 \times 10^6$ km^3 of material is excavated during crater formation in both scenarios, consistent with estimates based on crustal thickness modelling [14].

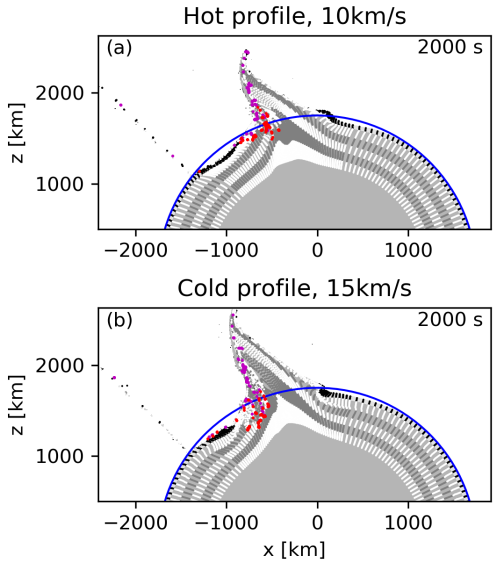

Figure 2: Comparison of simulations with different thermal gradients at time of maximum uplift. Colours are the same as Figure 1. Blue circle shows pre-impact surface.

Differences between the hot and cold scenarios are observed that may allow discrimination between them based on comparison with geophysical observations. The central uplift in the cold case extends several hundred km higher than in the hot case because of the higher impact energy (Figure 2). Even though the crater is smaller in the hot case, antipodal deformation is more extreme in the crust and upper mantle owing to the the latter's much lower strength in this scenario.

Acknowledgements: We thank the developers of iSALE (isale-code.de), in particular Oskar Thoren, Lorenzo Paganelli and Athena Elafrou. TMD and GSC were funded by STFC grant ST/S000615/1. This work was performed using the DiRAC Data Intensive service at Leicester, operated by the University of Leicester IT Services, part of the STFC DiRAC HPC Facility (www.dirac.ac.uk). The equipment was funded by BEIS capital funding via STFC capital grants ST/K000373/1 and ST/R002363/1 and STFC DiRAC Operations grant ST/R001014/1. DiRAC is part of the National e-Infrastructure.

References: [1] Garrick-Bethell, I. & Zuber, M. T. (2009). *Icarus*, 204:399–408. [2] Moriarty, D. P. & Pieters, C. M. (2018). *JGR Planets*, 123:729–747. [3] James, P. B. et al. (2019). *Geophysical Research Letters*, 46:5100–5106. [4] Potter, R. W. K. et al. (2012). *Icarus*, 220:730–743. [5] Garrick-Bethell, I. et al. (2020). *Icarus*, 338:113430. [6] Wieczorek, M. A. et al. (2012). *Science*, 335:1212–1215. [7] Melosh, H. et al. (2017). *Geology*, 45:1063–1066. [8] Elbeshausen, D. et al. (2009). *Icarus*, 204:716–731. [9] Thompson, S. L. & Lauson, H. S. (1972). *Sandia National Laboratory Report*, SC-RR-71 0:309p. [10] Benz, W. et al. (1989). *Icarus*, 81:113–131. [11] Pierazzo, E. et al. (1997). *Icarus*, 127:408–423. [12] Ivanov, B. A. et al. (2010). *Geol. Soc. Spec. Pap.* 465:29–49. [13] Petro, N. E. & Pieters, C. M. (2002). *LPSC XXXIII Proc.* 1848. [14] Wieczorek, M. A. & Phillips, R. J. (1999). *Icarus*, 139:246–259.